SCIENCE CHINA
Chemistry

•COMMUNICATIONS•

https://doi.org/10.1007/s11426-022-1513-8

Predictably synthesizing a library of white-light-emitting perovskites

Ludan Niu[1†], Lili Zhao[2†], Deyu Li[1], Qian Chen[1], Mingming Zhang[1], Jing Luan[3], Lei Wang[1,4], Weigao Xu[2*] & Jun Xing[1*]

[1]*Key Laboratory of Eco-chemical Engineering, Ministry of Education, College of Chemistry and Molecular Engineering, Qingdao University of Science & Technology, Qingdao 266042, China;*
[2]*Key Laboratory of Mesoscopic Chemistry, Ministry of Education, School of Chemistry and Chemical Engineering, Nanjing University, Nanjing 210023, China;*
[3]*School of Materials Science and Technology, Qingdao University of Science & Technology, Qingdao 266042, China;*
[4]*Shandong Engineering Research Center for Marine Environment Corrosion and Safety Protection, College of Environment and Safety Engineering, Qingdao University of Science and Technology, Qingdao 266042, China*

Received September 30, 2022; accepted January 16, 2023; published online January 18, 2023

The low-dimensional organic-inorganic halide perovskites with self-trapped exciton emission have promising prospects for single-phase white-light emitters. However, so far, these broadband white-light-emitting (BWLE) perovskites were synthesized by trial-and-error testing spacing molecules. Here, we developed a steric hindrance regulation strategy to predictably synthesize BWLE perovskites. The molecules containing C–C(–NH_2)–C groups were introduced into low-dimensional perovskites, which brings a large steric hindrance in-plane orientation. The bigger C–C(–NH_2)–C bond angle would induce larger structural distortion in perovskites, which leads to the higher rate of self-trapping of excitons and the deeper self-trapping depth. The photoluminescence spectra of the synthesized perovskites can cover the cool-to-warm white light region. Overall, we fabricated a material library consisting of 40 kinds of BWLE compounds according to this strategy. Our findings develop a general strategy to synthesize BWLE perovskites and offer a material platform for optoelectronic applications.

white-light emission, halide perovskite, steric hindrance, two-dimensional

Citation: Niu L, Zhao L, Li D, Chen Q, Zhang M, Luan J, Wang L, Xu W, Xing J. Predictably synthesizing a library of white-light-emitting perovskites. *Sci China Chem*, 2023, 66, https://doi.org/10.1007/s11426-022-1513-8

Nowadays, white-light-emitting diodes (LEDs) are widely used for artificial lighting. The traditional white LEDs contain multiple color emitters, which suffer from color instability and efficiency loss due to different degradation rates and overlapping absorption of the emitters. Thus, developing single-emitters with broadband white-light emission is necessary for lighting applications [1–4]. Recently, low-dimensional organic-inorganic hybrid perovskites emitting broadband white light emerge as an interesting candidate and show promising prospects for single-component white-light emitters. It was firstly proposed in a two-dimensional (2D) perovskite by Karunadasa *et al*. [5,6]. Hereafter, some BWLE perovskites were discovered [2,7–12]. The broadband emission arises from self-trapped excitons (STEs), which are photogenerated in the deformable lattice associated with the strong electron−phonon coupling [13–16]. Although it is generally recognized that the structural distortion in the inorganic layers of perovskites plays a key role in determining the self-trapping of excitons [8,9,17–21], the origin of the structural distortion is not yet clear. So far, the reported organic-inorganic hybrid BWLE perovskites have

†These authors contributed equally to this work.
*Corresponding authors (email: xuwg@nju.edu.cn; xingjun@qust.edu.cn)

been synthesized by screening the spacing organic molecules. Therefore, it is highly desirable to develop a design strategy for the direct synthesis of BWLE perovskites.

Herein, we reveal the effect of molecular configuration on the structural distortion of perovskites and pioneer a steric hindrance regulation strategy to predictably synthesize BWLE perovskites. Typically, the spacing molecules containing C–C(–NH_2)–C groups were applied to synthesize 2D perovskites, which bring a large steric hindrance in the in-plane orientation and induce the structural distortion. The degree of the structural distortion in the perovskite could be regulated by controlling the C–C(–NH_2)–C bond angle of the molecule, which determines the self-trapping of free excitons (FEs). The synthesized perovskites exhibit the tunable broadband emission covering from 400 to 800 nm, and the bigger molecular steric hindrance induces the larger structural distortion and the higher self-trapping rate of excitons, which, therefore, results in the cool- to warm-white-light. According to this strategy, we can extend the functional molecules to secondary and tertiary amines with the group of C–NH_x–C, and successfully fabricate 40 kinds of perovskites with the broadband emission. Our studies open a general way to the direct synthesis of abundant BWLE perovskites and uncover the relationship of molecular steric hindrance–structural distortion–STEs in the perovskites.

2D bromide-based perovskites are the most commonly obtained BWLE perovskites [11]. For the prototypical (100)-oriented 2D bromide-based perovskite, it can be considered as the crystallographic layer slicing along (100) planes of the parent three-dimensional perovskite, and $PbBr_6$ octahedrons are connected by sharing corners to form layered frameworks [11]. The inorganic framework layers are spaced by long-chain organic ammonium (R–NH_3^+) layers, and the R–NH_3^+ cations are embedded into the interstitial space of the four adjacent $PbBr_6$ octahedrons by the attractive Coulomb force between R–NH_3^+ and $PbBr_6^{4-}$. Due to the steric hindrance effect, the molecular configuration involving the bond angle and length of the alkyl group bonding to –NH_3^+ would influence the structure of the inorganic framework in perovskites [8,9,17].

Thus, cyclopropylamine (*c*-C_3), cyclobutylamine (*c*-C_4), cyclopentylamine (*c*-C_5), cyclohexylamine (*c*-C_6), isopropylamine (2-C_3), and sec-butylamine (2-C_4) with different bond angles were used as spacing molecules to fabricate perovskite crystals. We synthesized the 2D lead-bromide-based perovskite single-crystals by the reported anti-solvent diffusion method (see Supporting Information for detailed experiments) [12,22]. As shown in Figure 1a, the C–C(–NH_2)–C bond angle of *c*-C_3 is 60.0°. As the size of the carbocycle increases, the C–C(–NH_2)–C bond angle gradually increases to 111.6° for *c*-C_6, which is close to the bond angle (109.4°) of molecule 2-C_3 and 2-C_4. In the perovskite framework, we denote the bridging Br atoms in the in-plane direction and terminal Br atoms in the out-of-plane direction as Br_{in} and Br_{out}, respectively (Figure S1). When these molecules are inserted into the inorganic framework to form 2D perovskites, the group C–C(–NH_2)–C with a big bond angle would induce large steric hindrance in the in-plane direction and push aside the neighboring Br_{out} atoms. In the tightly packed layers, the $PbBr_6$ octahedrons consequently distort to tolerate the geometric constraints, which may occur on Pb–Br bond length or angle variation.

Firstly, single-crystal X-ray diffraction (XRD) measurements were performed at room temperature to monitor the structural changes of these perovskite crystals. As shown in Figure 1b, all these plate-shaped perovskite crystals feature layered structures, and organic ammoniums are inserted into the perovskite framework with the general formula (R–NH_3)$_2$$PbBr_4$. The perovskites of *c*-C_3, *c*-C_4, and *c*-C_5 crystalize in the monoclinic space group with the lattice parameter (β) decreasing from 108.9° to 108.0° and 106.2°, while *c*-C_6, 2-C_3 and 2-C_4 belong to the orthorhombic space group (Table 1 and Tables S1–S6). The product of lattice parameters, *b* and *c*, as well as the Pb–Br_{in} bond length of the perovskites can be approximately considered as the lattice expansion in the in-plane orientation, which approximately increases as the C–C(–NH_2)–C bond angle of the spacing molecules increases. The powder XRD measurements were performed to confirm the purity of these crystals (Figure S2). The molecules, *n*-propylamine (1-C_3), *n*-butylamine (1-C_4), cyclopropylmethylamine (*c*-C_3MA), cyclobutylmethylamine (*c*-C_4MA), cyclopentylmethylamine (*c*-C_5MA), and cyclohexylmethylamine (*c*-C_6MA), were used to synthesize the controlled perovskites which have only H–C(–NH_2)–C group (Figure 1a and Figure S3). Due to the C–H bond length of about 1.09 Å being much shorter than the C–C bond length of about 1.54 Å, the steric hindrance in the in-plane direction of the 2D perovskite caused by the group H–C(–NH_2)–C should be much smaller than that of C–C(–NH_2)–C.

To ascertain the effect of molecular steric hindrance on the structural distortion of perovskites, we determined the degree of the structural distortion by calculating the distortion level of $PbBr_6$ octahedrons as following equation (1): [9,17,19,23–25]

$$\Delta d = \frac{1}{6}\sum_{i=1}^{6}\left(\frac{d_i - d}{d}\right)^2 \quad (1)$$

where d is defined as the average Pb–Br bond length of $PbBr_6$ octahedrons, and d_i are the six individual Pb–Br bond lengths. The Pb–Br bond length and the corresponding Δd of these perovskites are summarized in Table 1. The molecular configuration turns out to be the crucial factor leading to the structural distortion of the perovskites. In general, as the molecular steric hindrance increases, the Pb–Br_{in} bonds would be stretched. Nevertheless, the Pb–Br_{out} bonds would be compressed. According to the above analysis, we can

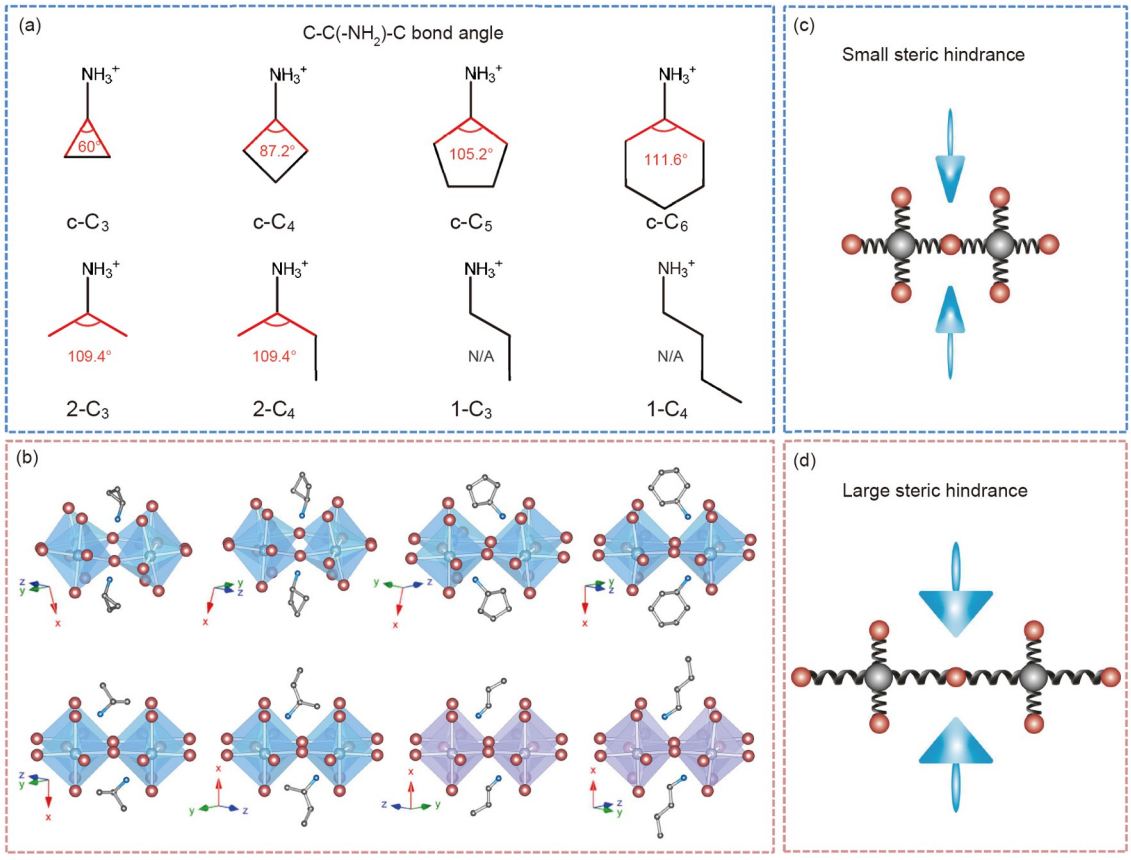

Figure 1 (a) Configuration of the molecules of *c*-$C_{3/4/5/6}$, 2-$C_{3/4}$, and 1-$C_{3/4}$. The C–C(–NH_2)–C means the medium carbon atom bonds to the –NH_2 group, which is represented with red lines. (b) The crystal structures of the corresponding lead-bromide-based perovskites. Red balls (Br), blue/violet balls (Pb), grey balls (C), and blue balls (N). Hydrogen atoms are omitted for clarity. (c, d) The schematic of the molecular steric effect on the chemical structure of perovskites. Red balls (Br), grey balls (Pb), blue arrows (alkylammniums) (color online).

Table 1 Crystal structure data of the perovskites and their corresponding optical characteristics

	c-C_3	*c*-C_4	*c*-C_5	*c*-C_6	2-C_3	2-C_4 [a)]	1-C_3	1-C_4 [22]
Crystal system	monoclinic	monoclinic	monoclinic	orthorhombic	orthorhombic	orthorhombic	orthorhombic	orthorhombic
a (Å)	12.402	13.247	13.502	27.930	23.419	25.679	25.126	27.617
b (Å)	7.990	8.197	8.091	8.623	8.367	8.368	8.294	8.223
c (Å)	8.335	8.337	8.803	8.365	8.444	8.358	8.209	8.334
α (°)	90	90	90	90	90	90	90	90
β (°)	108.879	107.948	106.225	90	90	90	90	90
γ (°)	90	90	90	90	90	90	90	90
Pb–Br_{out} bond length (Å)	2.989 2.989	2.970 2.970	2.994 2.994	2.966 2.966	2.947 2.947	2.969 2.969	2.984 2.984	3.014 3.014
Pb–Br_{in} bond length (Å)	3.001 3.001 3.004 3.004	3.020 3.020 3.021 3.021	3.048 3.048 3.077 3.077	3.026 3.031 3.111 3.194	3.045 3.045 3.049 3.049	3.048 3.048 3.048 3.048	2.990 2.990 3.000 3.000	2.995 2.995 3.003 3.003
Δd	4.7×10^{-6}	6.3×10^{-5}	1.3×10^{-4}	7.1×10^{-4}	2.5×10^{-4}	1.5×10^{-4}	5.0×10^{-6}	6.7×10^{-6}
PL I_{STEs}/I_{FEs}	0.9	4.9	10.1	115.5	13.3	42.6	0.8	0.4
ΔG (eV)	0.73	0.84	0.86	1.07	0.86	1.15	0.61	0.58

a) All single-crystal XRD measurements were performed at room temperature, except perovskite 2-C_4 at 150 K.

picture the steric effect on the chemical structure of perovskites (Figure 1c, d). The controlled perovskites, 1-C_3, 1-C_4, and *c*-$C_{3/4/5/6}$–MA, with the only H–C(–NH_2)–C bond have Δd of about 10^{-6} which is one or two orders of mag-

nitude smaller than that of the perovskites containing C–C(–NH_2)–C bonds (Table 1 and Table S7). The larger C–C(–NH_2)–C bond angle, the bigger Δd. Especially, the single-crystal structure data from the perovskite of 2-C_4 can be only collected at low temperature (150 K), which may be due to the serious vibration of the molecule at room temperature. At low temperatures, the long Pb–Br_{in} bond of the distorted $PbBr_6$ octahedrons would shrink, while the short Pb–Br_{out} bond would expand, which would cause the decrease of the Δd value compared with that at room temperature (Note S1) [26].

In 2D lead-bromide-based perovskites, the quantum confinement effect mainly determines their bandgaps. Usually, the 2D bromide-based perovskites always display an excitonic absorption band at about 400 nm, and the non-absorption at longer wavelengths, which is also observed on all as-synthesized perovskites (Figure 2a). As expected, the controlled perovskites, 1-C_3, 1-C_4, and *c*-$C_{3/4/5/6}$MA, with the negligible distortion show a sharp narrowband FE-related emission (FWHM=12–14 nm) at about 410 nm and the negligible broadband STE-related emission with a large Stokes shift (Figure 2a and Figure S4). Similar photoluminescence (PL) spectrum is also obtained on the perovskite of *c*-C_3 with the little structural distortion. However, as Δd of the perovskite increases, the PL intensity of the broadband STE-related emission increases accordingly on the perovskites of *c*-$C_{4/5/6}$ and 2-$C_{3/4}$. The average ratio of the STE-related emission to FE-related emission (I_{STEs}/I_{FEs}) is around 0.9, 5.0, 10.0, 115.5, 13.3, and 42.6 for the perovskites of *c*-C_3, *c*-C_4, *c*-C_5, *c*-C_6, 2-C_3, and 2-C_4, respectively, which have a linear relationship with the structural distortion of perovskites (Figure 2b). For the perovskite of *c*-$C_{3/4}$, their FE-related emissions exhibit an asymmetric band spectrum. The low-energy shoulder peak at about 415–430 nm can be attributed to the repabsorption of the FE-related emission in the thick plate-shaped perovskite crystals [22]. As shown in Figure 4, such perovskites with overall broadband PL spectra from 400 to 800 nm can cover from the cold- to warm-white light region. The PL quantum yields (PLQYs) of *c*-$C_{3/4/5/6}$ and 2-$C_{3/4}$ are measured to be about 9%, 9%, 11%, 2%, 3% and 5%, respectively (Table S10). Besides, it should be noted that bond angle variance and out-of-plane tilting of the $PbBr_6$ interoctahedral could not be key factors for the self-trapping of excitons, because the Pb–Br bonds of $PbBr_6$ octahedrons might be elongated or compressed without leading to bond angle changes and out-of-plane tilting. For example, the perovskite of 2-$C_{3/4}$ display a large Δd, while their Br–Pb–Br bond angles nearly remain 90º and have no out-of-plane tilting of the $PbBr_6$ interoctahedral . (Table S8).

Interestingly, some needle-shaped crystals also grow in the 2-C_4 product, which crystallizes in the 9R polytype with a formula of $(C_4H_{12}N)_4Pb_3Br_{10}$, being analogous with reported $(tms)_4Pb_3Br_{10}$ and $(tmpa)_4Pb_3Br_{10}$ (tms: trimethylsulfonium;, tmpa: trimethylphenylammonium) [27–29]. The trimers of face-sharing octahedrons assemble into Pb–Br layers through sharing corners (Figure S5). The distortion-related PL spectra are also evidenced on the needle-shaped crystal of 2-C_4, which has an average Δd of 9.4×10^{-4} and correspondingly exhibits a similar PL spectrum to the plate-shaped crystal of 2-C_4 (Table S9 and Figure S6).

We confirmed the origin of the broadband STE-related

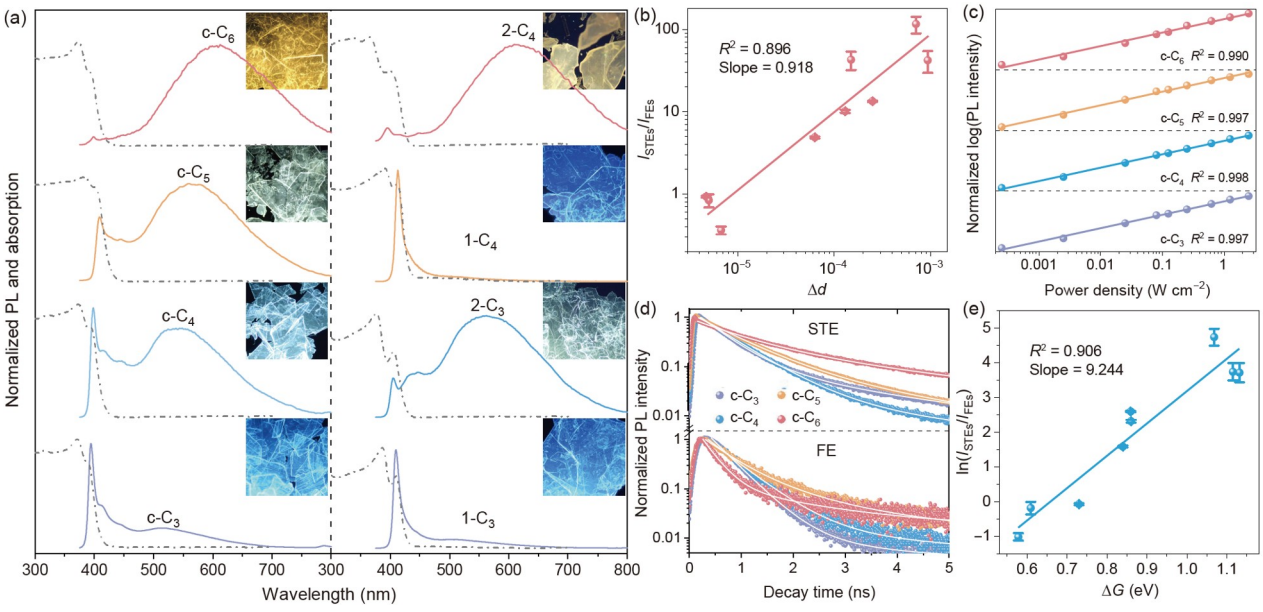

Figure 2 (a) Normalized absorption (grey lines) and PL spectra (color lines) of *c*-$C_{3/4/5/6}$, 1-$C_{3/4}$, and 2-$C_{3/4}$. Insets are the fluorescence images of the corresponding crystals. (b) The emission ratio (I_{STEs}/I_{FEs}) of *c*-$C_{3/4/5/6}$, 1-$C_{3/4}$ and 2-$C_{3/4}$ with different Δd. (c) Normalized excitation power-dependent PL intensities of *c*-C3/4/5/6. (d) PL decay profiles of FE- and STE-related emissions of *c*-$C_{3/4/5/6}$ under the excitation power of 4.3 mW. (e) The curve of $\ln(I_{STEs}/I_{FEs})$ *versus* $\Delta G_{self\text{-}trap}$ of *c*-$C_{3/4/5/6}$, 1-$C_{3/4}$ and 2-$C_{3/4}$ (color online).

emission by implementing power-dependent PL measurement, which shows a linear dependence from 0.00025 to 2.5 W cm^{-2} under femtosecond-pulse laser irradiation (Figure 2c). If the broadband PL originates from permanent defects, it usually shows sublinear power dependence with the saturation of limit defect sites under high excitation intensity (Note S2). Moreover, the power-dependent PL lifetime was detected without significant difference, and there is no PL signal observed on the perovskite samples under sub-band-gap energy excitation (450, 508 and 663 nm laser), which further precludes the defect-derived broadband emission of these perovskites (Figure S7 and Table S11). The defect-derived broadband emission can also be ruled out by comparing the PL spectra of perovskite bulk single-crystals and powders synthesized *via* the fast reprecipitation method (see the Supporting Information for experimental details). The powders of *c*-$C_{3/4/5/6}$ show much lower PLQY than that of their corresponding single crystals (Table S10), while they have very similar PL spectra as single crystals (Figure S8). Noticeably, for the perovskite of *c*-C_3, a weak STE-related PL spectrum centered at about 513 nm accompanies a small PL intensity ratio of I_{STEs}/I_{FEs}. As the ratio of I_{STEs}/I_{FEs} successively increases on the perovskites of *c*-C_4, *c*-C_5, and *c*-C_6, their STE-related PL peak locations redshift from about 543 to 569 and 608 nm correspondingly. Figure 2d illustrates the PL lifetime of these perovskites of *c*-$C_{3/4/5/6}$. The PL decay curves can be well fitted with a bi-exponential decay model. The fast-decay and slow-decay components can be attributed to the non-radiative and radiative processes, respectively, which give a short lifetime (τ_1) and a long lifetime (τ_2) (Table S11). The radiative PL lifetimes derived from FE- and STE-related emission of perovskites of *c*-$C_{3/4/5/6}$ are around 2 ns and 2–3 ns, respectively. According to the previous report [30], the thermodynamic equilibrium between FEs and STEs can be determined by the following equation (2, 3), the emission ratio of I_{STEs}/I_{FEs} is related to $\Delta G_{self\text{-}trap}$ and the radiative emission rates from the STE- and FE-related states ($k_{r,STEs}$ and $k_{r,FEs}$).

$$\frac{I_{STEs}}{I_{FEs}} \propto \frac{k_{r,STEs}}{k_{r,FEs}} \exp\left(-\frac{\Delta G_{self\text{-}trap}}{k_B T}\right) \quad (2)$$

In this case, the STE-related states in these perovskites are several hundreds of meV lower than the FE-related states. Thus,

$$\frac{I_{STEs}}{I_{FEs}} \propto \frac{\tau_{r,FEs}}{\tau_{r,SFEs}} - \frac{\Delta G_{self\text{-}trap}}{k_B T} \approx \frac{\Delta G_{self\text{-}trap}}{25.3\ \text{meV}} (T = 293\text{K}) \quad (3)$$

Here, we assume the energy gap between the FE- and STE-related emission peak as the corresponding $\Delta G_{self\text{-}trap}$. As expected, the ratios of $\ln(I_{STEs}/I_{FEs})$ show a linear relationship with $\Delta G_{self\text{-}trap}$ for these perovskites at room temperature (Figure 2e), which verifies the relationship experimentally.

Figure 3a–d show the temperature-dependent PL spectra of perovskite *c*-$C_{3/4/5/6}$. When the temperature decreases from 293 to 77 K, the FE-related emission peaks blueshift gra-

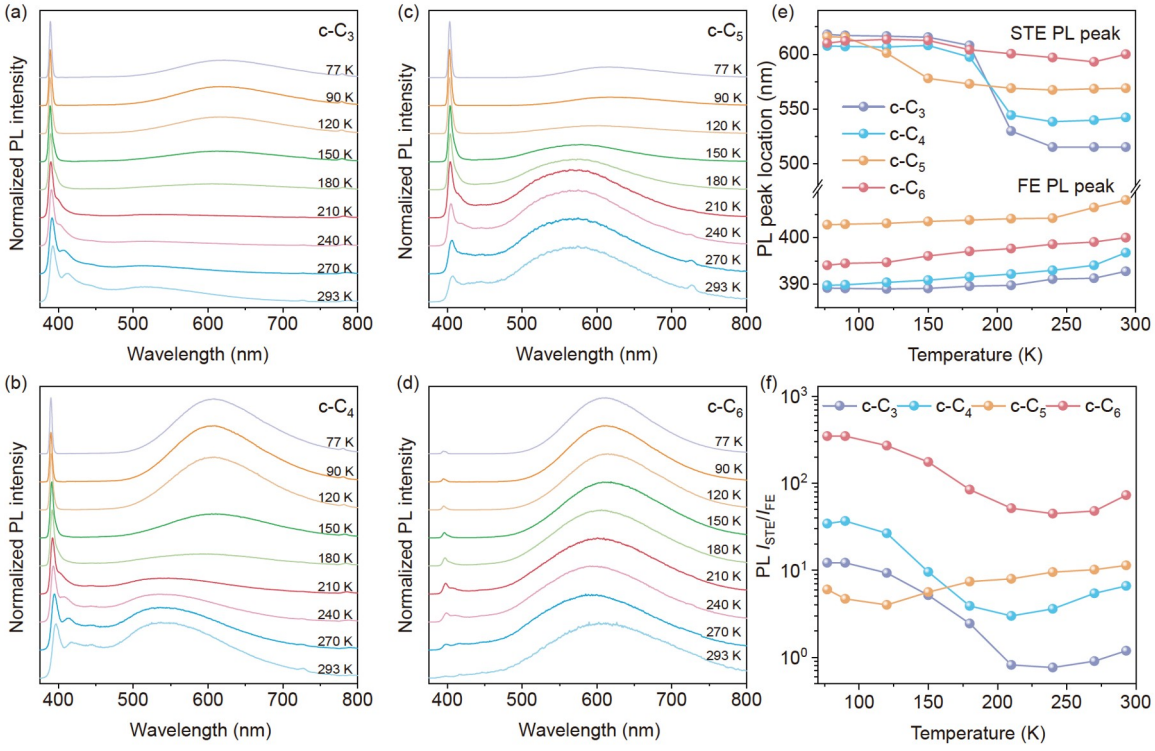

Figure 3 (a–d) Temperature-dependent PL spectra of *c*-$C_{3/4/5/6}$ from 298 to 77 K. The signals at about 730 and 800 nm in PL spectra are the frequency-doubled reflection peak of 365 nm excitation light and FE-related emission. (e) Temperature-dependent PL peak and (f) PL intensity ratio of I_{STEs}/I_{FEs} of *c*-$C_{3/4/5/6}$ (color online).

dually, which can be attributed to the lattice shrinking and bandgap increasing at low temperatures. Meanwhile, the STE-related emission peaks suddenly redshift at 180–210 K for *c*-$C_{3/4/6}$ and 120–150 K for *c*-C_5. The crystal structure of these perovskites shows no phase transition from 293 to 173 K (Table 1 and Note S1). However, as mentioned above, the Pb–Br_{in} bond would shrink and the Pb–Br_{out} bond would stretch as cooling, which might influence the lattice vibration in perovskite crystals and consequently affect the electron–phonon coupling at the critical temperature. The ratio of I_{STEs}/I_{FEs} at low temperatures would be determined by the self-trapping and de-trapping process of FEs. At the initial cooling process, the I_{STEs}/I_{FEs} of *c*-$C_{3/4/5/6}$ decreases, which may be due to the weak exciton–phonon interaction and the suppressed the self-trapping of FEs at low temperatures. The I_{STEs}/I_{FEs} inversely increases from 180–210 K for *c*-$C_{3/4/6}$ and around 90 K for *c*-C_5, probably because the self-trapping of FEs is enhanced and the detrapping of STEs is reduced as $\Delta G_{self\text{-}trap}$ increases significantly at the critical temperature. As shown in Figure S9, the reduced electron–phonon interaction at low temperatures would narrow the FWHM of both FE- and STE-related emission spectra generally. Meanwhile, the FWHM of the STE-related emission increases at the critical temperature of STEs emission redshift, 210 K for *c*-$C_{3/4}$ and 120 K for *c*-C_5. It can be concluded that the crystal structures of the perovskite change in the cooling process, which brings the stronger electron–phonon coupling at the critical temperature and alters the optical characteristics.

Furthermore, to verify the general application of this synthesis strategy, we fabricated the organic-inorganic hybrid compounds by applying more primary amines with large C–C(–NH_2)–C bond angles. No surprise, all these compounds display broadband emissions. Likewise, molecules containing secondary amines (C–NH–C) or tertiary amines (C–N(–C)–C) groups bring larger steric hindrances than those containing primary amines, and the broadband white-light emissions were also obtained on their corresponding compounds. These molecules and their corresponding PL spectra and CIE chromaticity coordinates of these compounds are summarized in Figures 4, 5, S10 and S11. We summarized the I_{STEs}/I_{FEs} and $\Delta G_{self\text{-}trap}$ of these compounds, which is well matched with the exponential relationship mentioned above (Figure S12a). The crystal structures of compound 8, 9, 10 and 13 have been reported [31–34] and we also obtained the single-crystal structures of compound 6, 27, 29 with the well crystalline quality. As shown in Figure S13, compound 13 and 29 exhibit a 2D perovskite structure, and the $PbBr_6$ octahedrons are connected by the corner-sharing. The compound 8, 9, 10 exhibit an one-dimensional structure, and the $PbBr_6$ octahedrons are connected by the

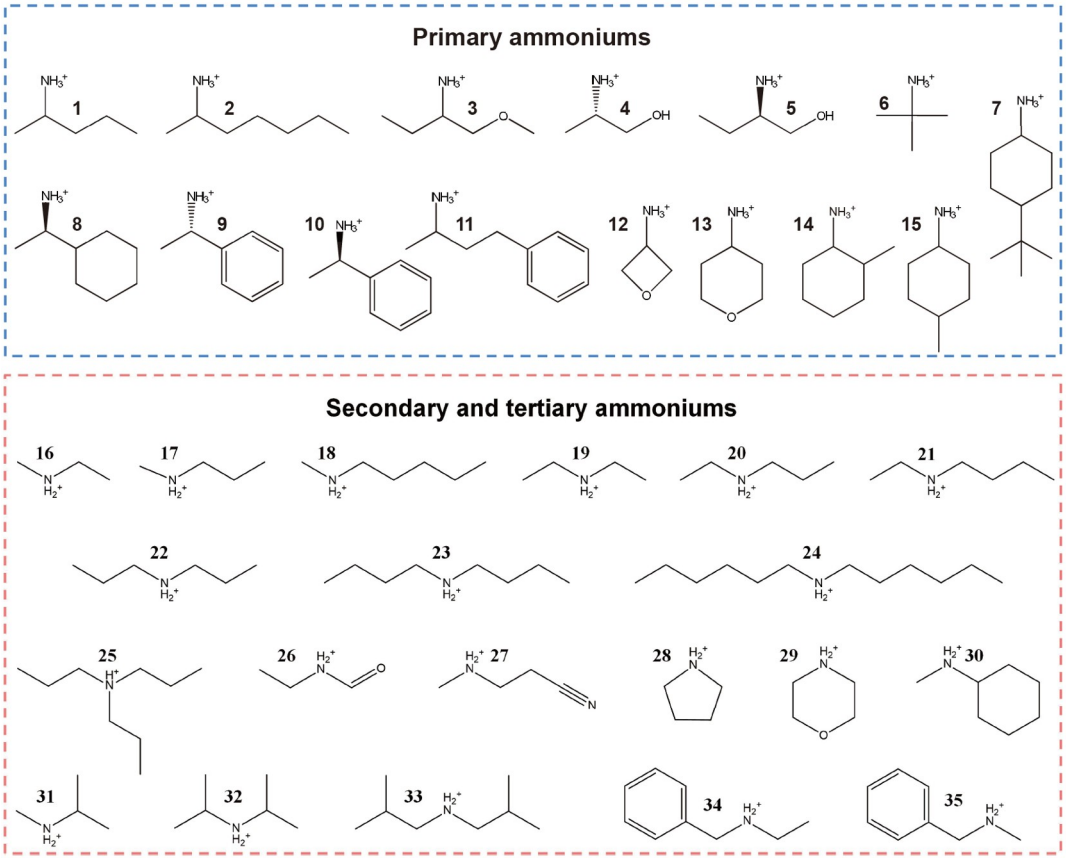

Figure 4 The configuration of the molecules applied to synthesize broadband emitting compounds (color online).

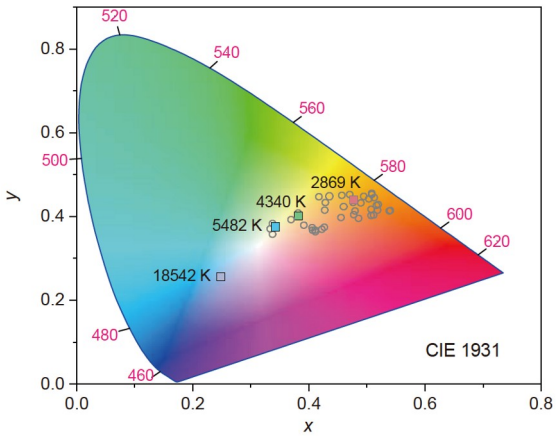

Figure 5 The emission color of the compounds. CIE chromaticity coordinates of the emission of perovskites of *c*-C_3 (purple square), *c*-C_4 (blue square), *c*-C_5 (green square), *c*-C_6 (red square), other compounds (grey cycles). The color temperatures are corresponding to *c*-$C_{3/4/5/6}$ (color online).

face-sharing. The compound 6 and 27 also exhibit a 2D structure, but Pb atoms coordinate with 8 Br atoms to form hendecahedrons which are connected by the face-sharing. We also calculated their PL ratios of I_{STEs}/I_{FEs}, which are approximately proportional to the structural distortions (Table S12, Figure S12b). Although some of the compounds are not perovskite-type, they are still in the rule of the structural distortion inducing the self-tapping of excitons. The PLQYs of compound 7, 13, 15, 22, 29 are 4%, 12%, 20%, 11%, 17%, respectively. Other compounds exhibit low PLQY of <1%. The non-radiative recombination of excitons is mainly attributed to the defect-trapping- and electron–phonon coupling-induced decay. On the one hand, the distortion-free perovskites of 1-$C_{3/4}$ display higher PLQY than most of the distorted perovskites (Table S10), because lots of defects incline to form to relax the inner stress of the crystal with the distorted structure. On the other hand, the cyclic ammonium-based perovskites show a higher PLQY than the linear ammonium-based perovskites, due to the relatively weak electron–phonon coupling in the perovskite composed of rigid molecules.

In summary, we developed a steric hindrance regulation strategy to predictably synthesize the BWLE perovskites. The spacing molecules induced the intrinsic distortion was revealed in the perovskites and the distortion-related self-trapping of excitons was evidenced by detecting the STE-related emission in perovskites with the controllable distortion. Self-trapping excitons follow the Arrhenius relationship, and their self-trapping depth determines the emission ratio of I_{STEs}/I_{FEs}. Based on our findings, we can speculate that (1) under photoexcited conditions, the crystal lattice of perovskites would be polarized; in the dynamic process of the polarization, the inner stress in distorted $PbBr_6$ octahedral units might drive the distorted structure to restore to the distortion-free structure, namely deformed lattice; the localized deformed lattice would produce a potential well and trap the free excitons, namely STEs. (2) The larger structural distortion might induce the heavier lattice deformation under light irradiation, which would generate the potential wells with lower energy and consequently trap more excitons. Thereby, the larger the structural distortion of perovskite, the lower the energy of the emission and the higher the PL intensity ratio of I_{STEs}/I_{FEs}. (3) The movement of the electron and hole determines the dynamic nature of the lattice polarization and the distributed energy level of the potential wells. As a result, the self-trapped excitons recombine and emit photons with distributed wavelength, namely broadband emission. Further investigations are required to fully understand and discover the nature of the formation and emission of STEs.

Acknowledgements J.X. acknowledges financial support from National Natural Science Foundation of China (21905154) and the Taishan Scholars Program. W.X. acknowledges the Fundamental Research Funds for the Central Universities in China (020514380231; 021014380177), the National Natural Science Foundation of China (22173044; 21873048), the National Key R&D Program of China No. 2020YFA0406104, "Innovation & Entrepreneurship Talents Plan" of Jiangsu Province.

Conflict of interest The authors declare no conflict of interest.

Supporting information The supporting information is available online at chem.scichina.com and link.springer.com/journal/11426. The supporting materials are published as submitted, without typesetting or editing. The responsibility for scientific accuracy and content remains entirely with the authors. The X-ray crystallographic coordinates for structures reported in this study have been deposited at the Cambridge Crystallographic Data Centre (2150592-2150603).

1 Chen J, Xiang H, Wang J, Wang R, Li Y, Shan Q, Xu X, Dong Y, Wei C, Zeng H. *ACS Nano*, 2021, 15: 17150–17174
2 Luo J, Wang X, Li S, Liu J, Guo Y, Niu G, Yao L, Fu Y, Gao L, Dong Q, Zhao C, Leng M, Ma F, Liang W, Wang L, Jin S, Han J, Zhang L, Etheridge J, Wang J, Yan Y, Sargent EH, Tang J. *Nature*, 2018, 563: 541–545
3 Chen J, Wang J, Xu X, Li J, Song J, Lan S, Liu S, Cai B, Han B, Precht JT, Ginger D, Zeng H. *Nat Photonics*, 2021, 15: 238–244
4 Xiang H, Wang R, Chen J, Li F, Zeng H. *Light Sci Appl*, 2021, 10: 206
5 Dohner ER, Hoke ET, Karunadasa HI. *J Am Chem Soc*, 2014, 136: 1718–1721
6 Dohner ER, Jaffe A, Bradshaw LR, Karunadasa HI. *J Am Chem Soc*, 2014, 136: 13154–13157
7 Yuan Z, Zhou C, Tian Y, Shu Y, Messier J, Wang JC, van de Burgt LJ, Kountouriotis K, Xin Y, Holt E, Schanze K, Clark R, Siegrist T, Ma B. *Nat Commun*, 2017, 8: 14051
8 Mao L, Wu Y, Stoumpos CC, Wasielewski MR, Kanatzidis MG. *J Am Chem Soc*, 2017, 139: 5210–5215
9 Mao L, Guo P, Kepenekian M, Hadar I, Katan C, Even J, Schaller RD, Stoumpos CC, Kanatzidis MG. *J Am Chem Soc*, 2018, 140: 13078–13088
10 Gautier R, Massuyeau F, Galnon G, Paris M. *Adv Mater*, 2019, 31: 1807383
11 Smith MD, Connor BA, Karunadasa HI. *Chem Rev*, 2019, 119: 3104–3139

12 Zhang M, Zhao L, Xie J, Zhang Q, Wang X, Yaqoob N, Yin Z, Kaghazchi P, Zhang S, Li H, Zhang C, Wang L, Zhang L, Xu W, Xing J. *Nat Commun*, 2021, 12: 4890
13 Song KS, Williams RT. *Self-trapped Excitons*. Berlin:Springer, 1993
14 Tao W, Zhang C, Zhou Q, Zhao Y, Zhu H. *Nat Commun*, 2021, 12: 1400
15 Thomaz JE, Lindquist KP, Karunadasa HI, Fayer MD. *J Am Chem Soc*, 2020, 142: 16622–16631
16 Hu T, Smith MD, Dohner ER, Sher MJ, Wu X, Trinh MT, Fisher A, Corbett J, Zhu XY, Karunadasa HI, Lindenberg AM. *J Phys Chem Lett*, 2016, 7: 2258–2263
17 Li X, Guo P, Kepenekian M, Hadar I, Katan C, Even J, Stoumpos CC, Schaller RD, Kanatzidis MG. *Chem Mater*, 2019, 31: 3582–3590
18 Ji C, Wang S, Li L, Sun Z, Hong M, Luo J. *Adv Funct Mater*, 2019, 29: 1805038
19 Febriansyah B, Giovanni D, Ramesh S, Koh TM, Li Y, Sum TC, Mathews N, England J. *J Mater Chem C*, 2020, 8: 889–893
20 Han Y, Li Y, Wang Y, Cao G, Yue S, Zhang L, Cui BB, Chen Q. *Adv Opt Mater*, 2020, 8: 1902051
21 Wang X, Meng W, Liao W, Wang J, Xiong RG, Yan Y. *J Phys Chem Lett*, 2019, 10: 501–506
22 Gong X, Voznyy O, Jain A, Liu W, Sabatini R, Piontkowski Z, Walters G, Bappi G, Nokhrin S, Bushuyev O, Yuan M, Comin R, McCamant D, Kelley SO, Sargent EH. *Nat Mater*, 2018, 17: 550–556
23 Lufaso MW, Woodward PM. *Acta Crystlogr B Struct Sci*, 2004, 60: 10–20
24 Li D, Wu W, Wang S, Zhang X, Li L, Yao Y, Peng Y, Luo J. *J Mater Chem C*, 2020, 8: 6710–6714
25 Wang S, Yao Y, Wu Z, Peng Y, Li L, Luo J. *J Mater Chem C*, 2018, 6: 12267–12272
26 Billing DG, Lemmerer A. *CrystEngComm*, 2009, 11: 1549–1562
27 Stoumpos CC, Mao L, Malliakas CD, Kanatzidis MG. *Inorg Chem*, 2017, 56: 56–73
28 Smith MD, Watson BL, Dauskardt RH, Karunadasa HI. *Chem Mater*, 2017, 29: 7083–7087
29 Wiest T, Blachnik R, Reuter H. *Z für Naturforschung B*, 1999, 54: 1099–1102
30 Smith MD, Jaffe A, Dohner ER, Lindenberg AM, Karunadasa HI. *Chem Sci*, 2017, 8: 4497–4504
31 Lemmerer A, Billing DG. *S Afr J Chem*, 2013, 66: 262–272
32 Billing DG, Lemmerer A. *Acta Crystlogr E Struct Rep Online*, 2003, 59: m381–m383
33 Billing DG, Lemmerer A. *CrystEngComm*, 2006, 8: 686–695
34 Chen XG, Song XJ, Zhang ZX, Li PF, Ge JZ, Tang YY, Gao JX, Zhang WY, Fu DW, You YM, Xiong RG. *J Am Chem Soc*, 2020, 142: 1077–1082